











# Multiscale computational model predicts how environmental changes and treatments affect microvascular remodeling in fibrotic disease

Julie Leonard-Duke <sup>a,b</sup>, Samuel M. J. Agro <sup>c</sup>, David J. Csordas <sup>a,b</sup>, Anthony C. Bruce<sup>a</sup>, Taylor G. Eggertsen <sup>a,b</sup>, Tara N. Tavakol<sup>a</sup>, Tien Comlekoglu <sup>a</sup>, Thomas H. Barker <sup>a,b</sup>, Catherine A. Bonham <sup>d</sup>, Jeffrey J. Saucerman <sup>a,b</sup>, Lakeshia J. Taite <sup>c</sup> and Shayn M. Peirce <sup>a,b,\*</sup>

<sup>a</sup>Department of Biomedical Engineering, University of Virginia, Charlottesville, VA 22908, USA

<sup>b</sup>Robert M. Berne Cardiovascular Research Center, University of Virginia, Charlottesville, VA 22908, USA

<sup>c</sup>Department of Chemical Engineering, University of Virginia, Charlottesville, VA 22903, USA

<sup>d</sup>Department of Pulmonary and Critical Care Medicine, University of Virginia, Charlottesville, VA 22908, USA

\*To whom correspondence should be addressed: Email: [Smp6p@virginia.edu](mailto:Smp6p@virginia.edu)

Edited By Dennis Discher

## Abstract

Investigating the molecular, cellular, and tissue-level changes caused by disease, and the effects of pharmacological treatments across these biological scales, necessitates the use of multiscale computational modeling in combination with experimentation. Many diseases dynamically alter the tissue microenvironment in ways that trigger microvascular network remodeling, which leads to the expansion or regression of microvessel networks. When microvessels undergo remodeling in idiopathic pulmonary fibrosis (IPF), functional gas exchange is impaired and lung function declines. We integrated a multiscale computational model with independent experiments to investigate how combinations of biomechanical and biochemical cues in IPF alter cell fate decisions leading to microvascular remodeling. Our computational model predicted that extracellular matrix (ECM) stiffening reduced microvessel area, which was accompanied by physical uncoupling of endothelial cell (EC) and pericytes, the cells that comprise microvessels. Nintedanib, an Food and Drug Administration-approved drug for treating IPF, was predicted to further potentiate microvessel regression by decreasing the percentage of quiescent pericytes while increasing the percentage of pericytes undergoing pericyte-myofibroblast transition in high ECM stiffnesses. Importantly, the model suggested that YAP/TAZ inhibition may overcome the deleterious effects of nintedanib by promoting EC-pericyte coupling and maintaining microvessel homeostasis. Overall, our combination of computational and experimental modeling can predict and explain how cell decisions affect tissue changes during disease and in response to treatments.

**Keywords:** pericytes, endothelial cells, stiffness, idiopathic pulmonary fibrosis, modeling

## Significance Statement

The summation of cell fate decisions made by individual cells over time in response to combinations of intracellular, intercellular, and environmental cues can result in emergent, surprising, and sometimes deleterious tissue remodeling responses. In fibrotic disease, such as idiopathic pulmonary fibrosis (IPF), the molecular cues that drive cell fates can become disrupted. We paired a multiscale computational model with independent experiments to investigate how combinations of biomechanical and biochemical cues in IPF alter cell fate decisions leading to aberrant remodeling of the microcirculation. We found that increased environmental stiffness disrupted signaling in vascular cells in a manner that caused microvessel regression, and treatment with an Food and Drug Administration-approved drug for IPF surprisingly exacerbated this effect.

## Introduction

Cell fate decisions are dictated by combinations of intracellular, intercellular, and environmental cues. The summation of cell fate decisions made by individual cells in a tissue results in an emergent tissue response, such as an expanded, or regressed, microvascular network. Multiscale computational models allow

us to investigate how intersecting intracellular and extracellular cues combine to drive cell behaviors that ultimately generate tissue-level outcomes (1). Our group previously developed a multiscale computational model by combining agent-based modeling (ABM) of multiple cells in a population with logic-based ordinary differential equations modeling of intracellular signaling

**Competing Interest:** The authors declare no competing interests.

**Received:** May 9, 2024. **Accepted:** November 13, 2024

© The Author(s) 2024. Published by Oxford University Press on behalf of National Academy of Sciences. This is an Open Access article distributed under the terms of the Creative Commons Attribution-NonCommercial License (<https://creativecommons.org/licenses/by-nc/4.0/>), which permits non-commercial re-use, distribution, and reproduction in any medium, provided the original work is properly cited. For commercial re-use, please contact [reprints@oup.com](mailto:reprints@oup.com) for reprints and translation rights for reprints. All other permissions can be obtained through our RightsLink service via the Permissions link on the article page on our site—for further information please contact [journals.permissions@oup.com](mailto:journals.permissions@oup.com).

networks within each simulated cell (2). We used the model to predict how profibrotic growth factors and proinflammatory cytokines in a highly simplified, generic extracellular environment affect intracellular signaling within individual fibroblasts, causing them to secrete collagen. Inspired by that proof-of-concept work, we developed a new computational model and combined it with *in vitro* and *ex vivo* wet-lab experiments to study how intracellular signaling in heterogeneous, individual cells elicits cell fate decisions that dynamically drive microvascular remodeling in the context of fibrotic lung tissue.

Microvascular homeostasis and remodeling are mediated by interactions between the two cells that compromise the microvasculature, endothelial cells (ECs), and pericytes, the cells that physically enwrap ECs. EC–pericyte coupling in all tissues maintains microvascular homeostasis (3–7) and regulates immune cell trafficking (8–14). In the lung, EC–pericyte coupling is crucial for ensuring adequate blood perfusion (15–17) to enable the exchange of carbon dioxide (CO<sub>2</sub>) and oxygen (O<sub>2</sub>) across the alveolar interstitial space to support the lung’s primary function of gas exchange (18–20). However, when this microenvironment is perturbed due to disease or the introduction of a drug, individual cell fate decisions lead to cellular states that collectively give rise to tissue-level microvascular phenotypes. For example, in response to proangiogenic stimuli, ECs and pericytes temporarily uncouple from one another to allow for capillary sprouting and expansion of the microvascular network. ECs and pericytes subsequently recouple with one another to stabilize the newly formed capillaries (7, 21). In contrast, when antiangiogenic cues dominate, EC–pericyte uncoupling is typically followed by apoptosis of one or both cell types, leading to capillary regression, or the pruning of existing microvessels (7, 21).

Microvascular impairments in lung disease present clinically as a decline in the diffusion capacity for carbon monoxide. This occurs in idiopathic pulmonary fibrosis (IPF) (22), a progressive and fatal fibrotic disease of the lung characterized by heterogeneous formation of fibrotic foci throughout the lung. In the United States over 40,000 people are diagnosed with IPF annually with a mean survival rate of 2 to 3 years after diagnosis. Disease progression can be highly variable across patients, with some rapidly declining within a year of diagnosis while others decline slower across 5 to 6 years post-diagnosis (23–27). Thickening and stiffening of the interstitial space and loss of alveolar structures are thought to cause aberrant microvascular remodeling. However, reports of excessive, leaky vasculature conflict with reports of vascular regression (28–31), and the molecular drivers of EC and pericyte fates leading to dynamic remodeling of the microcirculation in this context are not well understood (32, 33).

Several growth factors that mediate EC–pericyte coupling are dysregulated in IPF, including VEGF-A, PDGF-BB, and Ang 1 & 2 (31, 34–40). In patients with IPF and animal models of IPF, pericytes decouple from ECs and express myofibroblast markers, such as collagen and alpha smooth muscle actin ( $\alpha$ SMA) (32, 33, 41). Importantly, the two Food and Drug Administration (FDA) approved drugs used to treat IPF, nintedanib, and pirfenidone, target key signaling pathways in ECs and pericytes. Nintedanib is of particular interest in this context, as it inhibits both vascular endothelial growth factor receptor (VEGFR), a key pro-survival and proangiogenic cue, and platelet-derived growth factor receptor (PDGFR), which is important for pericyte recruitment. Nintedanib also inhibits fibroblast growth factor receptor (FGFR), which is known to regulate angiogenesis and pericyte recruitment (42, 43). Additionally, fibrotic lesions, or foci, in IPF undergo progressive and spatially heterogeneous mechanical stiffening of the

extracellular matrix (ECM) (44), which can affect EC and pericyte dynamics (33, 45). Understanding how dysregulated biochemical and biomechanical signals impact EC–pericyte coupling in IPF necessitates the use of a computational model where the effects of these signals can be explored, both in isolation and in combination.

Here, we present a new multiscale computational model that combines ABM (2, 46–53) with logic-based ordinary differential equations modeling (54–57) to explore how biochemical and biomechanical signals integrate to affect EC and pericyte cell fate changes that give rise to structural microvascular adaptations in IPF (Fig. 1). Intracellular signaling in individual pericytes and ECs is represented by logic-based network models implemented in Netflux (54), while cell–cell communication, cell–environment communication, and tissue-level remodeling are represented by an ABM implemented in Netlogo (58). We used the model to predict microvascular remodeling in microenvironments with different mechanical stiffnesses that are characteristic of fibrotic foci, and experimentally validated these predictions with independent experiments. We then conducted a comprehensive set of *in silico* experiments by co-varying biomechanical and biochemical inputs, which yielded the novel prediction that nintedanib treatment in the presence of increased stiffness impairs EC–pericyte coupling by potentiating EC apoptosis and pericyte-to-myofibroblast transition (PMT). Finally, we use the model to identify a signaling pathway that could be therapeutically targeted to mitigate the potentially harmful effects of nintedanib on EC–pericyte coupling. Our combination of multiscale computational modeling with experiments provides new insights into how cellular phenotypic states driven by biomechanical and biochemical stimuli integrate to cause tissue-level changes in disease and in response to drug treatments.

## Results

### EC and pericyte intracellular signaling models and experimental validation

Two logic-based network models of the intracellular signaling networks within ECs (Fig. 2A) and pericytes (Fig. 2B) that regulate cell fate decisions, such as migration, apoptosis, and quiescence, were developed in Netflux (54). First, signaling pathways that were central to EC cell fate decision, such as VEGFR2, a major regulator of EC quiescence and proliferation (74), or pericyte cell fate decision, and PDGFR $\beta$ , which is a regulator of pericyte quiescence and migration (21), were identified through literature curation and then combined with other cell type specific pathways to construct a network diagram. Each protein, mRNA, or cell fate decision was represented as a “node” in network diagram, while the causal connections between the nodes (representing downstream signals) were represented by “edges.” The network model diagram was then converted to an ordinary differential equation-based (ODE) model using Netflux (54). Briefly, ODE equations were solved using a normalized Hill ODE to represent the activity of each node in the model with default parameters and logic gating, thus allowing inputs to be scaled from 0 to 1. For ECs, network outputs were simplified to represent three cell fate decisions: angiogenic, apoptotic, and quiescent. These cell states collectively contribute to microvessel network (tissue-level) outcomes, including microvessel remodeling that leads to expansion of the microvascular network, microvessel remodeling that leads to reduction of the microvascular network, and homeostasis (the absence of microvessel remodeling). In total, the EC model includes 32 species, 7 inputs, 32 reactions, and 3 cell fate outputs. Network outputs for the pericyte model represents three cell

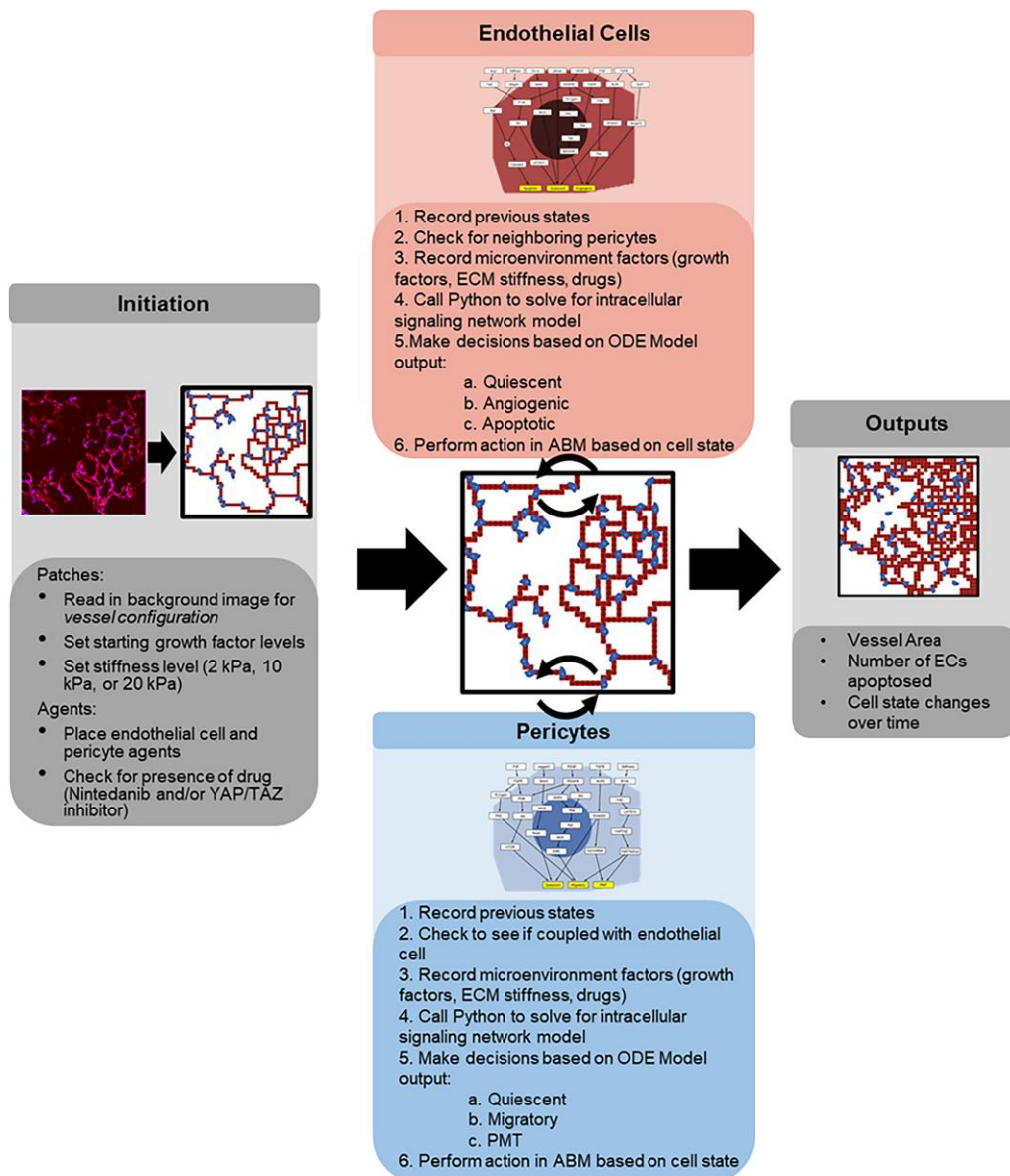


**Fig. 1.** Graphical abstract of multiscale model workflow. The initial model layout is approximated from an immunofluorescent image and starting values for environmental factors are set. Every timestep each agent in the model records its current microenvironment (growth factor levels, ECM stiffness, drug presence) and sends that information to a logic-based network model of intracellular signaling. The network model is solved and returns a cell state which the agent should adopt. This cycle repeats for 28 time steps (equivalent to 1 week of simulated time), and vessel remodeling outputs are recorded.

fate decisions: migratory, PMT, and quiescent. The pericyte model includes 32 species, 5 inputs, 34 reactions, and 3 cell fate outputs.

To validate the EC and pericyte models of intracellular signaling, predictions from both models (Fig. 2C and D) were compared to published experiments independent from those used to develop the models. A literature search was conducted to identify publications describing an experiment with ECs, pericytes, or a combination thereof, and a perturbation of interest, such as dosing with transforming growth factor beta (TGF $\beta$ ). The analogous simulation was then performed in Netflux by changing the input weight,  $w$ , of an equation from its baseline value to a value that represented the effect of the perturbation. For example, to validate the response to high levels of TGF $\beta$  in both EC and pericyte models, the input weight for TGF $\beta$ ,  $w_{\text{TGF}\beta}$ , was increased from baseline (0.35) to 0.5 and changes in relative activation of the output node were quantified and compared to the baseline relative activation. These qualitative changes in node activity were

then compared to their corresponding experimental findings. Since high TGF $\beta$  was predicted by the pericyte intracellular signaling model to increase PMT, and the corresponding experiment also demonstrated increased levels of PMT, as evidenced by  $\alpha$ SMA and Collagen 1 expression (45), we concluded that the model prediction matched the experiment. We further validated that under baseline conditions our models were not overly sensitive to any one input, and we explored the effect of high ECM stiffness on network sensitivity (Fig. S1).

### Mechanistic sub-network analysis suggests nintedanib regulates EC and pericyte phenotypes through similar pathways

Nintedanib is a receptor tyrosine kinase inhibitor that prevents phosphorylation of VEGFR, PDGFR, and FGFR, all three of which are expressed by ECs or pericytes and regulate microvascular

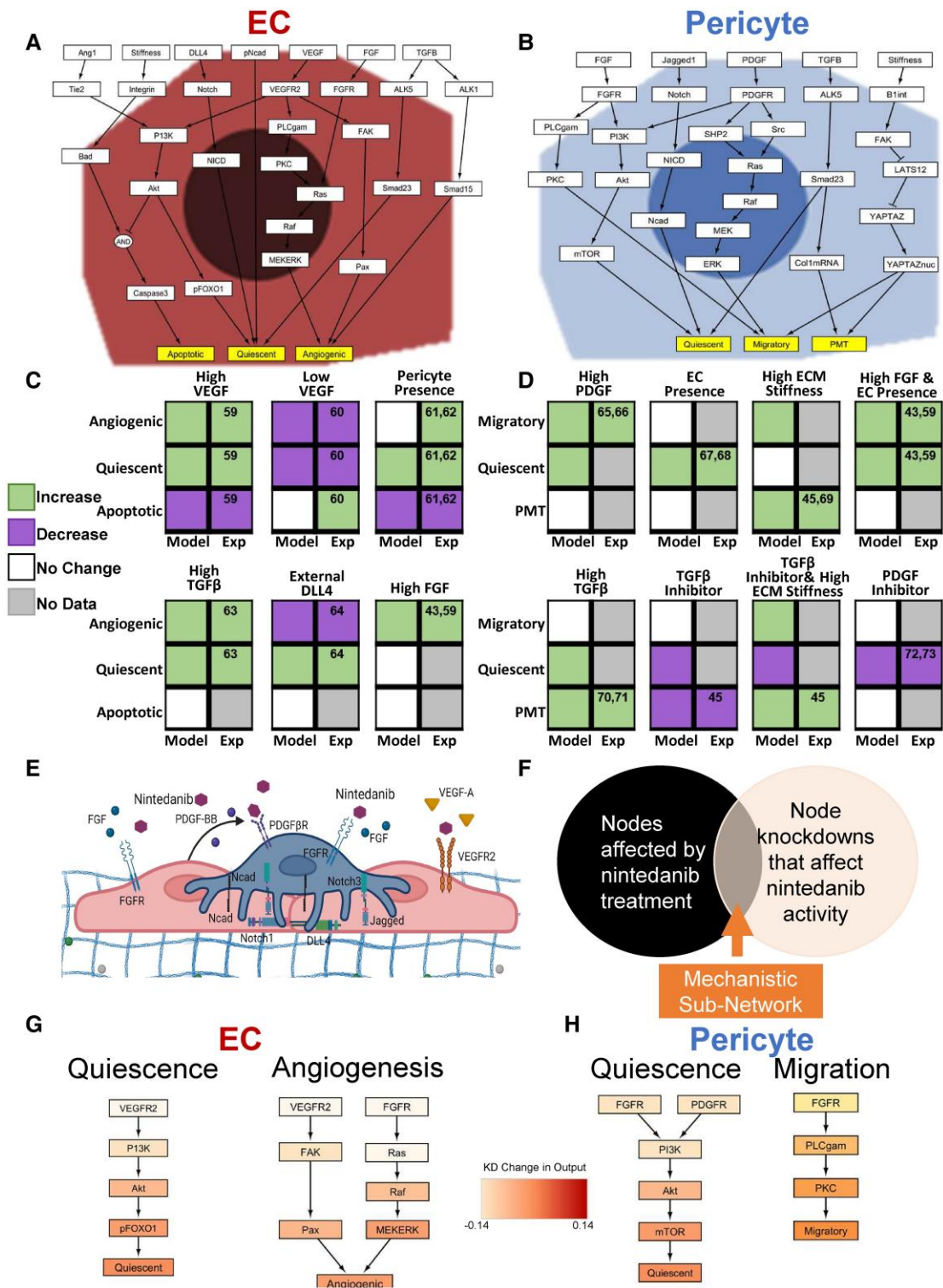


**Fig. 2.** EC and pericyte intracellular network signaling model predictions compared to published literature. A) EC network model and B) pericyte network model where each white box represents a specific signaling node (i.e. protein, transcription factor, or gene), and each yellow box represents a cell state change. C) Predictions of the EC network model (“Model” column) of cell fates resulting from six cellular and environmental perturbations relevant to IPF, including high (59) and low VEGF (60), contact with a neighboring pericyte (pericyte presence) (61, 62), high TGFβ (63), contact with a neighboring tip EC (presence of external DLL4) (64), and high FGF (43, 59) were compared to published experiments not used for model development (“Exp” column). 12 of 14 (85%) model predictions agreed with experimental outputs. D) Predictions of the pericyte network model (“Model” column) of cell fates resulting from eight cellular and environmental perturbations relevant to IPF, including high concentrations of PDGF-BB (65, 66), pericyte contact with a neighboring EC (67, 68), high ECM stiffness (45, 69), high FGF & contact with an EC (EC presence) (43, 59), high concentrations of TGFβ (70, 71), TGFβ inhibitor (45), a combination TGFβ inhibitor and high ECM stiffness (45), and a PDGF inhibitor (72, 73). Nine of 9 (100%) model predictions agreed with published experiments (“Exp” column). E) Diagram depicting nintedanib targets, VEGFR, PDGFR, and FGFR. F) Overview of mechanistic sub-network analysis. G) Sub-network analysis of nintedanib regulation of EC phenotype. H) Sub-network analysis of pericyte response to nintedanib. Sub-figure (E) was created using [Biorender.com](#).

homeostasis (Fig. 2E). To explore the effects of nintedanib on ECs and pericytes individually, we performed a mechanistic sub-network analysis to identify which nodes in the model most influenced nintedanib's effects on cell fate. This analysis was performed in two parts. First, treatment with nintedanib was simulated by reducing the activation weights,  $w$ , of VEGFR, PDGFR, and FGFR by 90% from 1 to 0.1 and quantifying the change in network activity. Then, a sensitivity analysis was performed by sequentially reducing each node's weighting to zero ( $w_{\text{node}}=0$ ). The overlap of these two analyses were then determined, where nodes that both respond to nintedanib and whose knockdown affect the specified phenotype are determined to be in the "mechanistic sub-network" (Fig. 2F). These nodes are predominantly responsible for determining how nintedanib affects ECs and pericyte signaling and cell fate decisions in the model.

For both cell types, we focused our mechanistic sub-network analysis on the cell fate decisions that are reversible, unlike apoptosis for ECs or PMT in pericytes, which are considered terminally differentiated cell states in our model. Quiescence in both cell types was regulated by a PI3K dependent pathway, although this was activated by VEGFR in ECs and by a combination of FGFR and PDGFR in pericytes (Fig. 2G and H). In ECs, VEGFR also regulated nintedanib's control over the angiogenic state in conjunction with FGFR signaling, although through different pathways. FGFR regulated the angiogenic state primarily through the Ras/Raf/MEK/ERK pathway, as previously observed in the literature (75). VEGFR signaling, which is connected with several downstream pathways in our model leading to angiogenesis, had its strongest effect via the FAK/Paxillin pathway. For pericytes, FGFR was predicted to be the major regulator of pericyte migratory response to nintedanib.

### *Validation of the multiscale model's ability to predict microvascular remodeling in response to altered levels of mechanical stiffness in the microenvironment*

A multiscale computational model of the lung microvasculature was constructed by connecting both the EC and pericyte intracellular signaling network models described above to a 2D ABM of a lung microenvironment, where the locations of simulated ECs and pericytes were approximated from an immunofluorescence (IF) image of healthy lung microvasculature (Fig. 1). The ABM, representing  $500\ \mu\text{m} \times 500\ \mu\text{m}$  slice of lung tissue in a  $41 \times 41$  square grid of pixels (with each pixel representing  $12 \times 12$  microns), was built in NetLogo (58). The ABM contains information about the extracellular cues, such as ECM stiffness and growth factor concentrations, at each pixel location in the 2D model. The Py extension in NetLogo was used to connect the ABM model with the two Netflux models thereby generating a multiscale model that integrates intracellular cues and cell fate decisions. These intracellular cues and cell fate decisions were computed by the Netflux models for each simulated cell while tissue properties were computed by the ABM to predict changes in microvascular network architectures and population-level cell fate outcomes, such as number of apoptotic ECs or percent of pericytes that have undergone PMT.

At each time step in the ABM representing 6 h, the cellular agents sense and respond to their local extracellular cues, and signals from neighboring cells, and input them into the logic-based network model. For each cell agent, the network model computes the relative activation of the cell fate decision nodes, and the cell fate decision that has the highest relative activation is enacted by that cell in the ABM. Simulated ECs can be in an angiogenic, apoptotic, or quiescent state, and pericytes can remain quiescent, migrate, or undergo pericyte-to-myofibroblast transition. Over the

entire simulation time course (representing 7 days), microvessel network (tissue-level) outcomes emerge as a summation of these independent cell decisions. Fifteen experimental replicates were performed for each computational study.

To validate the multiscale model's ability to predict microvessel network remodeling in response to microenvironmental stiffnesses variations, we simulated the responses of ECs and pericytes to stiffnesses ranging from 2 to 20 kPa recapitulating the stiffness differentials in healthy vs. IPF lungs (44). The multiscale model predicted that as ECM stiffness increases from healthy lung (2 kPa), to immature fibrosis (10 kPa), and mature fibrosis (20 kPa), the extent of the microvessel network, quantified by vessel area, significantly decreases (Fig. 3A), and this was associated with significant increases in EC apoptosis (Fig. 3B). The mean vessel area at 2 kPa,  $47.6\% \pm 1.4$ , was higher than the initial vessel area of 23.5%, and the mean number of ECs that underwent apoptosis was  $8.7 \pm 4.0$ , indicating that some levels of homeostatic remodeling occurred (Fig. 3C). At 10 kPa, mean vessel area was  $44.2\% \pm 2.0$ , and mean number of apoptotic ECs increased to  $145.9 \pm 14.1$ . This indicates that some level of angiogenesis occurred to offset the microvessel regression caused by EC apoptosis. Contrastingly, at 20 kPa (mature fibrosis), the mean vessel area dropped to  $9.71\% \pm 0.5$ , and the average number of apoptotic ECs increased to  $229.5 \pm 8.8$ , resulting in almost complete regression of the vascular network (Fig. 3D).

To determine if these predictions were biologically accurate, we utilized a murine lung explant angiogenesis assay that we have previously developed (76). Lungs from mice expressing an endogenous pericyte lineage-tracing fluorescent reporter (abbreviated, TdTomato Myh11-Cre mice, and described in the Methods) were sliced into  $1\ \text{mm} \times 1\ \text{mm} \times 1\ \text{mm}$  explants and then individually plated onto 6 mm diameter poly(ethylene glycol) diacrylate (PEGDA) hydrogels containing a combination of PDGF-BB and FGF-2 and with one of three stiffnesses matching those simulated in the computational model: 2, 10, and 20 kPa (Fig. 3E). After 7 days of culture, the explants were imaged and scored based on the presence of organized microvessel sprouts (Fig. 3F) or disorganized cell infiltration (Fig. 3G), as we have published previously (76). As hydrogel stiffness increased, the percent of images containing microvessel sprouts significantly decreased. This result correlated with our multiscale computational modeling results indicating that increased ECM stiffness leads to a decrease in vascular structures (Fig. 3H).

### **Predicting changes in cell fate decisions over time in response to ECM stiffness**

One advantage of having a multiscale model is that we can explore how the underlying cell fate decisions that drive microvascular remodeling in different environments change over time. We quantified how many ECs and pericytes were predicted in each cell fate category for each step of our model for 2, 10, and 20 kPa. At 2 kPa, we observed an initial drop in the percentage of quiescent ECs that was accompanied by a spike in the number of angiogenic cells. However, the overall system returned to a steady state of 95% quiescent cells at approximately day 3 (Fig. 4A). Over 95% of pericytes in these simulations maintained a quiescent state with small spikes in the percent of migratory pericytes in the earlier time points, aligning with the return of higher levels of quiescence in ECs (Fig. 4B). In 10 kPa, we saw a similar disruption in the quiescent EC population but in this scenario, we observed both angiogenic ECs and apoptotic ECs, indicating variable responses to local environmental cues (Fig. 4C). The return of 95% of the ECs to a quiescent cell state occurred on

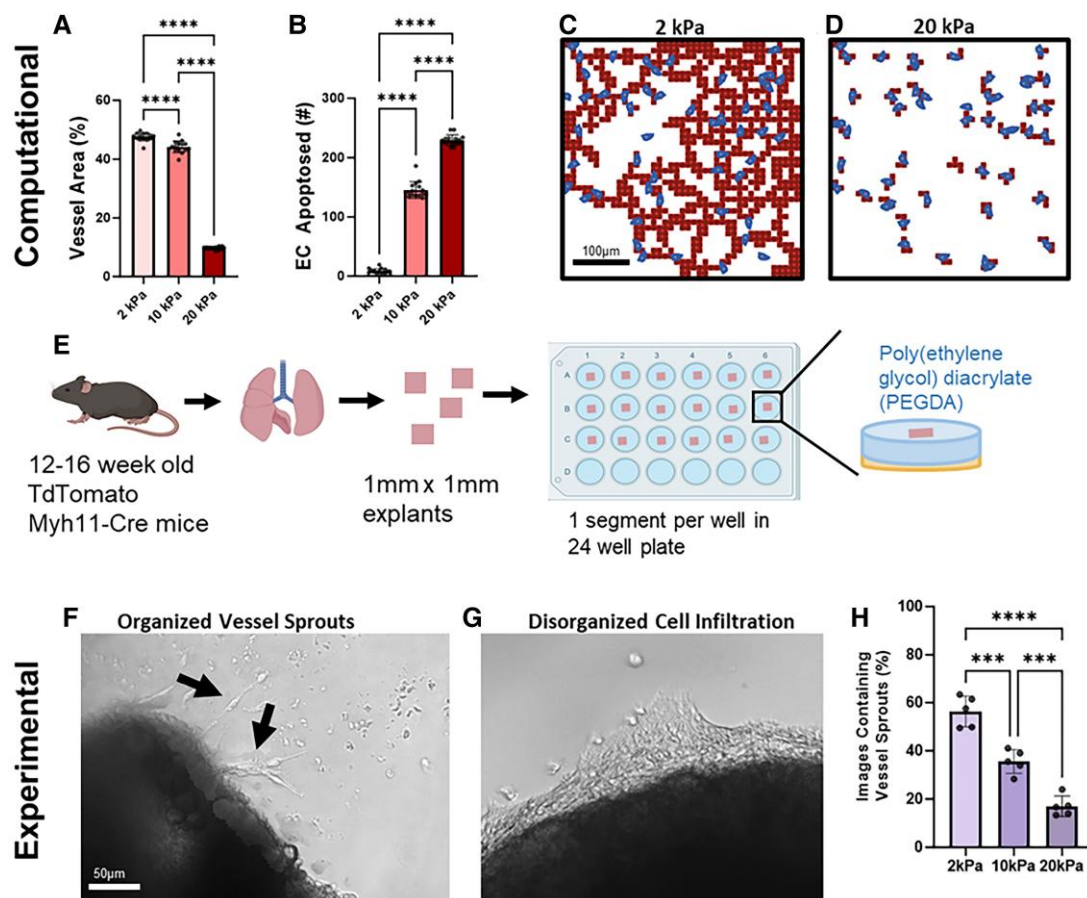


**Fig. 3.** Validation of multiscale model response to increasing stiffness. Computational results (A–D) and experimental results (E–H). Predicted blood vessel area as a percentage of total tissue area (A) and number of apoptotic ECs (B) at day 7 for different ECM stiffness levels.  $N = 15$  simulations per environmental stiffness condition representative model outputs at 2 kPa (C) and 20 kPa (D). E) Experimental design for lung explant assay. Representative brightfield microscopy image of the lung explant model with organized microvessel sprouts (F, black arrows) disorganized cell infiltration (G). H) Quantification of the number of images containing organized microvessel sprouts on day 7 for different ECM stiffness levels ( $N = 6$  samples per condition). One-way ANOVA with Tukey's post hoc test, \*\*\*\* $P < 0.001$ , \*\*\*\* $P < 0.0001$ . Parts of (E) were created using [Biorender.com](#).

day 6. In the 10 kPa microenvironment, we observed higher levels of migratory pericytes throughout the simulation, but over 95% of all pericytes maintained a quiescent steady state (Fig. 4D). In the 20 kPa microenvironment, the reduction in the percentage of quiescent ECs was accompanied by a large spike in the percentage of apoptotic ECs. However, the system quickly returned to a 95% quiescent cell steady state after 1 day, with occasional small spikes in apoptotic EC over the time course (Fig. 4E). Conversely, by day 3 fewer than 95% of pericytes were in a quiescent state, and they continued to decline over the simulation time course (Fig. 4F). This decline was accompanied by an increase in the percentage of migratory pericytes. Importantly, we also began to see low but persistent percentages of pericytes undergoing PMT at day 4.5.

### Predicting microvascular remodeling in variable stiffness environments in response to nintedanib

We next used the multiscale model to evaluate how treatment with nintedanib, one of two drugs FDA-approved for the treatment of IPF, affected microvascular remodeling in microenvironments with mechanical stiffnesses of 2, 10, and 20 kPa. Nintedanib inhibits VEGFR on ECs, PDGFR on pericytes, and FGFR, which is expressed by both cell types. Treatment with nintedanib was modeled by reducing the maximum activation weight of each receptor to 0.1 in both the EC and pericyte models. Based

on prior literature (77), we hypothesized that nintedanib would decrease vessel area in the computational model and microvessel infiltration into the hydrogel of the experimental model. Treatment with nintedanib resulted in significantly decreased vessel area in two of the three treated groups when compared to the untreated controls (Fig. 5A). At 2 kPa, significant decreases in vessel area ( $47.6\% \pm 1.4$  vs.  $44.0\% \pm 1.9$ ) were measured, although this was not associated with an increase in the number of apoptotic ECs ( $8.7 \pm 4.0$  vs.  $7.5 \pm 3.5$ ) (Fig. 5B). At 10 kPa, treatment with nintedanib reduced mean vessel area to  $41.9\% \pm 2.7$  compared to the control ( $44.2\% \pm 2.0$ ). Limited efficacy of nintedanib was observed at 20 kPa, as both groups had vessel areas of about 10% and no significant differences in number of apoptotic ECs.

Using the murine lung explant experimental model described above, we performed new experiments to determine if these model predictions were biologically accurate. After allowing sprouts to form for 7 days, lung explants were either treated with 50 nM nintedanib in 0.05% dimethylsulfoxide (DMSO) or 0.05% DMSO control. Seven days later, explants were imaged again and the amount of infiltration into the gel was quantified using an image analysis pipeline in Python. In summary, the image was imported and adaptive thresholding was used to create a mask that outlined the vascular infiltration in white and all other pixels were made black (Fig. 5D). The percent of white pixels in each image was calculated then averaged across each replicate for each

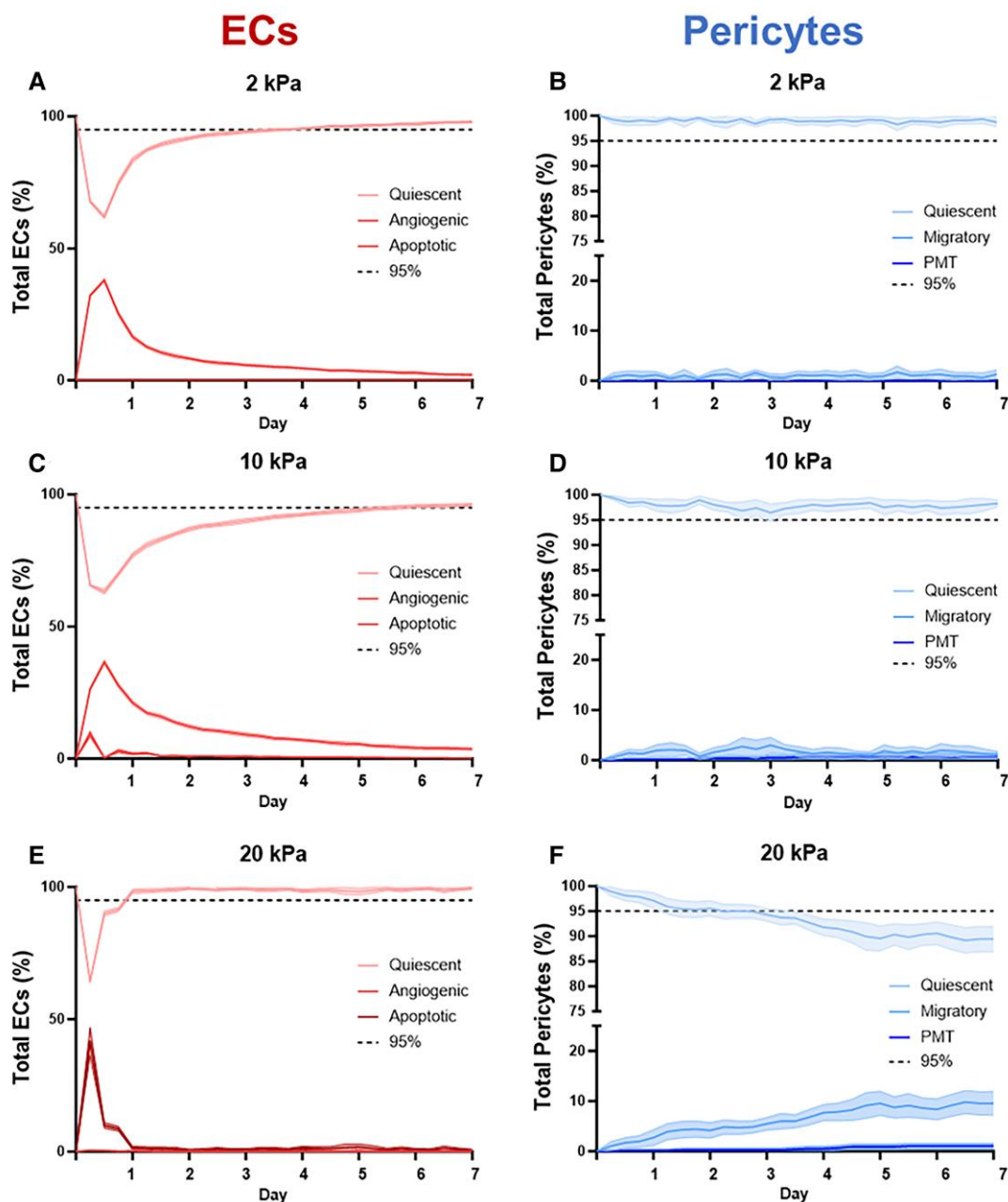


**Fig. 4.** Predicted effects of ECM stiffnesses on cell fate decisions over time. Percent of total ECs (A, C, E) predicted to be in a quiescent, angiogenic, or apoptotic state and percent of total pericytes (B, D, F) predicted to be in a quiescent, migratory, or PMT state in 2 kPa (A, B), 10 kPa (C, D), and 20 kPa (E, F) environments.  $N = 15$  simulations per environmental stiffness condition, shading represents 95% CI.

experimental group. At 2 kPa, the average percent infiltration across all explants treated with nintedanib was  $7.4 \pm 1.4$  which was lower than the DMSO-treated control group ( $10.7 \pm 1.4$ ) (Fig. 5C). Similar results were observed at 10 and 20 kPa, with the average infiltration category of the nintedanib-treated group ( $8.7 \pm 1.0$  in 10 kPa and  $7.6 \pm 0.7$  in 20 kPa) being significantly lower than the DMSO-treated control ( $11.8 \pm 1.5$  in 10 kPa and  $10.7 \pm 0.9$  in 20 kPa).

### Multiscale model predicts that nintedanib disrupts EC-pericyte coupling

EC and pericyte fate decisions at every time step were recorded for the simulations of nintedanib treatment in the microenvironments with different stiffnesses. While EC cell fate dynamics

were similar to those in the drug-free simulations, pericyte cell fate dynamics in the presence of nintedanib demonstrated a disruption in their coupling with ECs that was not predicted in the absence of drug.

In the 2 kPa microenvironment, the multiscale model predicted the same initial, transient drop below 95% in the percentage of quiescent ECs. The transient increase in angiogenesis that the model predicted without drug, also dissipated by day 3 in the presence of nintedanib (Fig. 6A). The pericyte dynamics in 2 kPa with nintedanib treatment were also similar to those in the absence of drug, with 95% of pericytes remaining in a quiescent steady state for the entire simulation duration (Fig. 6B). However, in microenvironmental stiffnesses of 10 kPa, we observed the first signs of impaired EC-pericyte coupling. While 95% of nintedanib-treated ECs returned to a quiescent state by day 5, slightly earlier

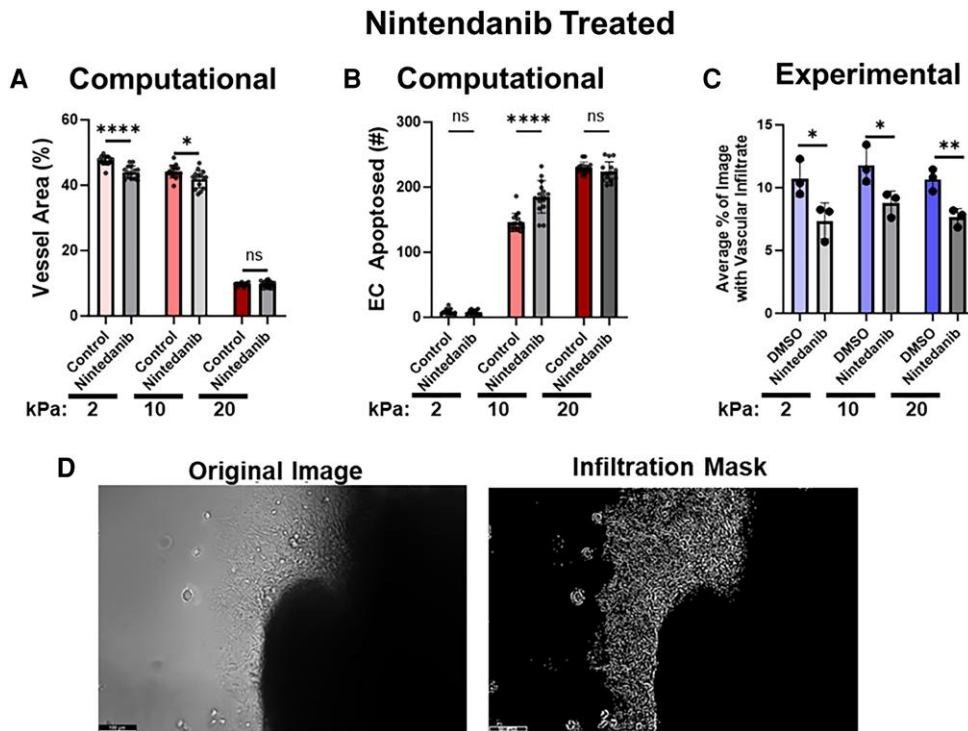


**Fig. 5.** Multiscale model predicts response to nintedanib. Predicted blood vessel area as a percentage of total tissue area (A) and number of apoptotic ECs (B) in the presence or absence of nintedanib in 2, 10, and 20 kPa stiffness levels on day 7 ( $N = 15$  simulations per condition). C) Percent of lung explant images on day 14 that contained vessels in the presence or absence of nintedanib in 2, 10, and 20 kPa stiffness levels ( $N = 3$  samples per group). D) Representative image of vascular infiltrate on day 14 and the image analysis mask used for quantification. Two-tailed t test, \* $P < 0.05$ , \*\* $P < 0.01$ , \*\*\*\* $P < 0.0001$ , ns, not significant.

than the drug-free simulations, the percentage of quiescent pericytes fell below 95% on day 4 and continued to decline over time (Fig. 6C and D). This loss of quiescence in pericytes was accompanied by an increase in PMT that was not seen in the absence of drug. Finally, in the 20 kPa microenvironment, the EC dynamics were predicted to be similar in both drug and drug-free simulations, with a spike in apoptosis and rapid loss of EC quiescence that were largely reversed by day 1 (Fig. 6E). Contrastingly, the model predicted a decline in the percentage of quiescent pericytes, which dropped below 95% as early as day 1 (compared to day 3 in the drug-free simulations) (Fig. 6F). This decline was concomitant with an increase in the percentage of migratory pericytes and earlier instances of pericytes adopting a PMT fate (at day 1 as opposed to day 4.5 in the drug-free simulation). On the individual cell level, nintedanib has a strong effect on both EC angiogenesis and quiescence in our sub-network model (Fig. 2G). Our simulations reveal, however, that on the multicellular level this impact is mitigated such that there are not drastic changes in the dynamics of ECs at the population level. Importantly, the sub-network analysis was also performed on a simulated EC without a neighboring pericyte. Therefore, it is possible that the presence of pericytes in the multicellular model mitigates the effects of nintedanib, as well. Because nintedanib targets three pathways, we wanted to dissect the role of the inhibition of each receptor in nintedanib-mediated loss of EC-pericyte coupling and vessel area (Fig. S2). In summary, treatment with a PDGFR inhibitor alone may be an ideal therapeutic strategy as it preserves EC-pericyte coupling at 10 kPa, delays the occurrence of PMT at 20 kPa, and prevents a stiffness-induced decrease in vessel area at 10 kPa.

### Multiscale model predicts a strategy to maintain EC-pericyte coupling in the presence of nintedanib

To identify a signaling pathway that could be targeted to mitigate the loss of vessel area caused by a stiff ECM and the increased percentage of pericytes exhibiting migratory and PMT states invoked by nintedanib treatment, we used the model to simulate inhibition of YAP/TAZ in the presence of nintedanib. In our model, the YAP/TAZ pathway is only present in pericytes and is upstream of both the migration and PMT cell state nodes. The pericyte network model was also found to be sensitive to YAP/TAZ knock out in the sensitivity analysis in Fig. S1. In the simulated 10 kPa microenvironment, treatment with both nintedanib and a YAP/TAZ inhibitor had no obvious effect on EC cell fate decisions (Fig. 7A); but the percentage of quiescent pericytes remained above 95% for the full 7-day time course (Fig. 7B). In contrast, in the pericyte response to nintedanib alone (Fig. 6D), the percentage of quiescent pericytes gradually decreased, starting on day 1, and dropped below 95% on day 5. In the simulated 20 kPa microenvironment, inhibition of YAP/TAZ decreased the height of the initial spike in the percentage of apoptotic ECs at day 0.5 (Fig. 7C) by approximately 20% compared to treatment with nintedanib alone (Fig. 6E). This was accompanied by a 1.5-day delay in the transition of pericyte states from the quiescent state to PMT and migratory states, which occurred at day 2.5 with the addition of YAP/TAZ inhibition (Fig. 7D) compared to day 1 in the nintedanib-alone simulation (Fig. 6F). Another difference caused by inhibition of YAP/TAZ was that the reduction in the percentage of pericytes in a quiescent state in the first half of the time course was associated with an increase in pericytes undergoing PMT. Contrastingly, this decrease in the nintedanib-alone simulation



## Nintendanib Treated

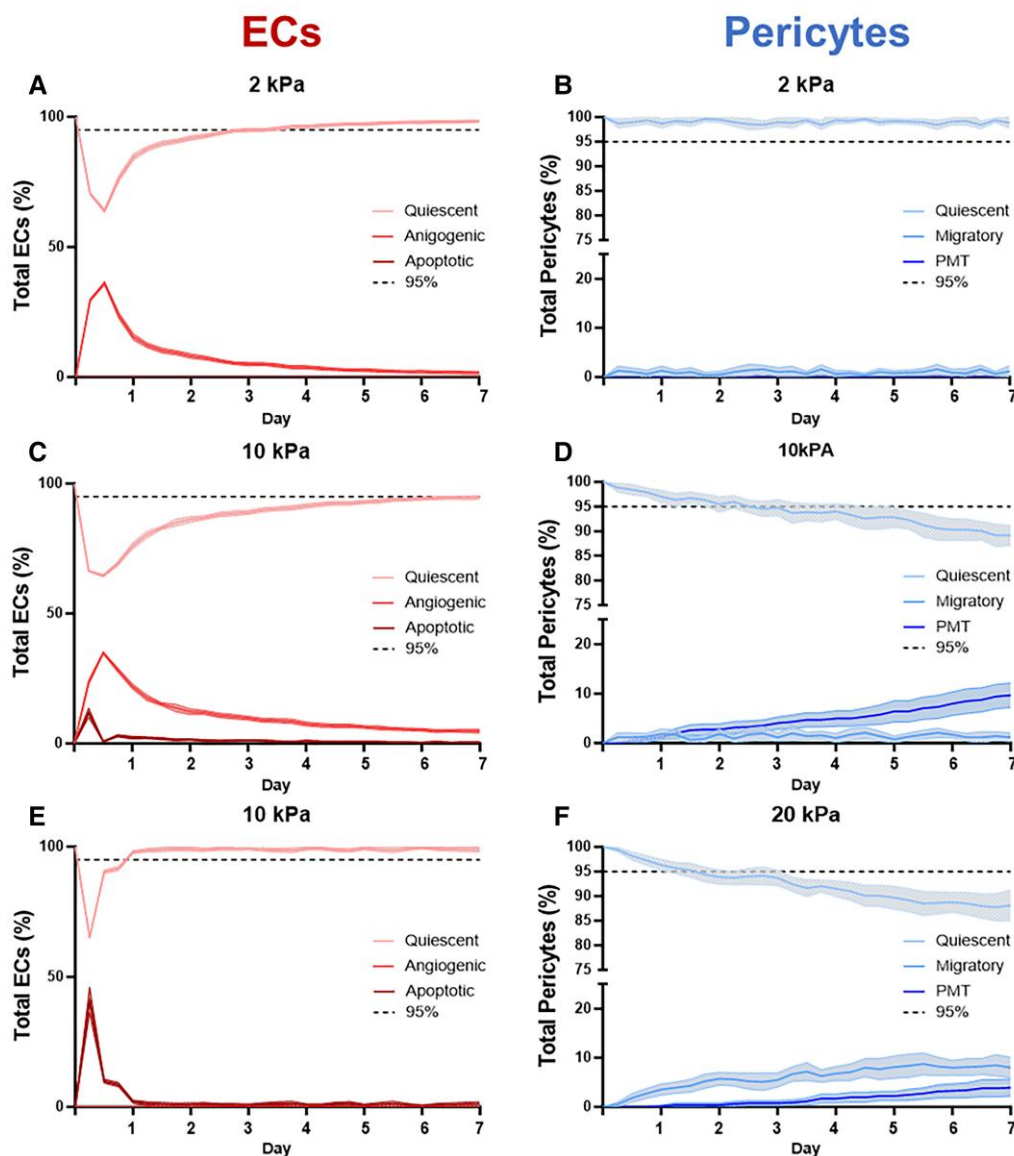


**Fig. 6.** Multiscale model predicts response to nintendanib over time. Percent of total ECs (A, C, E) predicted to be in a quiescent, angiogenic, or apoptotic state and percent of total pericytes (B, D, F) predicted to be in a quiescent, migratory, or PMT state in 2 kPa (A, B), 10 kPa (C, D), and 20 kPa (E, F) environments and when treated with nintendanib.  $N = 15$  simulations per environmental stiffness condition, shading represents 95% CI.

was more attributed to an increase in pericytes adopting a migratory state. The multiscale model predicted beneficial effects of these cell state changes on microvessel remodeling (Fig. 7E). By increasing the percentage of pericytes in a quiescent state in the simulated 10 kPa microenvironment, YAP/TAZ inhibition maintained microvessel area at levels that were similar to those in the 2 kPa microenvironment. However, this preservation of microvessel homeostasis with YAP/TAZ inhibition was not observed in the 20 kPa microenvironment. We also evaluated the effect of YAP/TAZ inhibition independent of nintendanib treatment and found it was able to maintain pericyte quiescence levels above 95% at all three simulated stiffnesses (Fig. S3).

## Discussion

Understanding mechanisms of disease and drugs across spatial scales—from molecule to tissue—remains a major challenge in

biomedical research that multiscale mechanistic modeling can help overcome. We demonstrate that a multiscale model can predict how the disease microenvironment and pharmaceuticals will interact, resulting in cell fate changes that affect tissue-level remodeling. We focused our study on IPF, where the impact of ECM stiffness on EC-pericyte coupling and microvascular remodeling are ambiguous, with conflicting reports of excess, leaky vasculature and regions void of any vasculature (31, 78–80). Our multiscale model's predictions of microvascular remodeling in response to altered mechanical stiffness alone, and in combination with nintendanib treatment, aligned with our experiments. Simulations suggested a new effect of nintendanib, which prevents EC-pericyte coupling in stiffer extracellular environments (10 and 20 kPa), thereby augmenting microvessel regression. These results are consistent with previous studies that observed decreased vessel area after nintendanib treatment in the bleomycin mouse model of IPF (81) and reduced association of ECs and mural cells

## Nintedanib +YAP/TAZ Inhibitor Treated

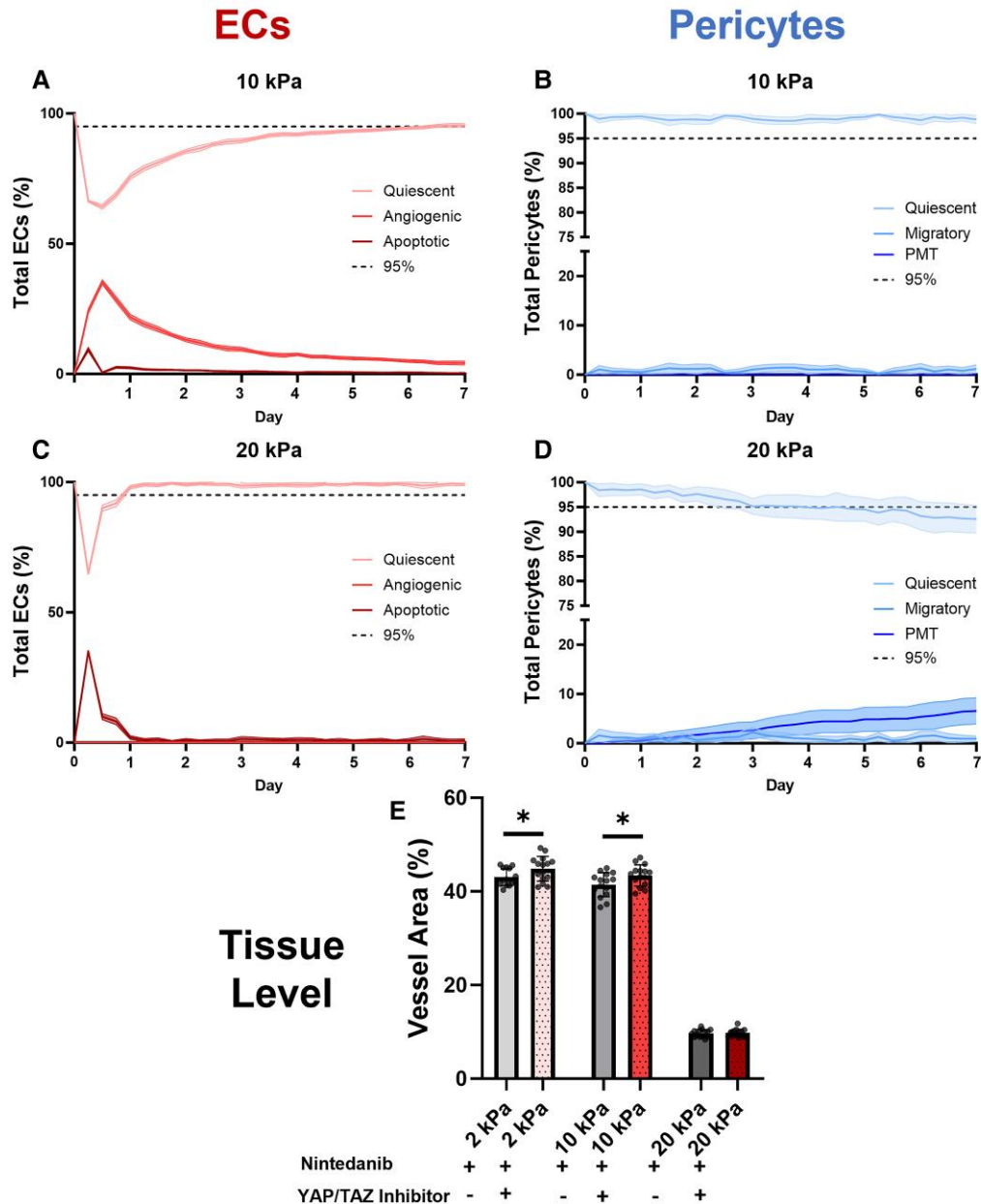


**Fig. 7.** Predicted effects of combined treatment with nintedanib and YAP/TAZ inhibition. Percent of total ECs (A, C) predicted to be in a quiescent, angiogenic, or apoptotic state and percent of total pericytes (B, D) predicted to be in a quiescent, migratory, or PMT state in 10 kPa (A, B) and 20 kPa (C, D) environments and when treated with nintedanib and YAP/TAZ inhibition.  $N = 15$  simulations per environmental stiffness condition, shading represents 95% CI. E) Predicted blood vessel area as a percentage of total area in the presence of nintedanib and with or without YAP/TAZ inhibition. Two-tailed t test,  $*P < 0.05$ .

in a co-culture model treated with nintedanib (77). Furthermore, when we used the multiscale model to identify a signaling pathway that can be targeted to preserve EC-pericyte coupling in stiffer environments, it suggested that inhibition of YAP/TAZ signaling can counteract the negative effects of nintedanib on EC-pericyte coupling prior to mature scar formation.

We started with a focus on the disease environment by using the multiscale model to investigate how the summation of individual EC and pericyte fate decisions in different microenvironmental stiffnesses impacted microvessel remodeling. At the cellular level, the model predicted how increasing ECM stiffness from 2 to 20 kPa contributed to a breakdown in communication between ECs and pericytes, as more ECs become apoptotic and

more pericytes exhibited a migratory cell state. This corresponded with our explant experimental results wherein stiff PEGDA hydrogels were sufficient to disrupt vessel sprouts. While stiffness is just one aspect of the dysregulated microenvironment in IPF, a stiff ECM alone can cause vascular regression (45). For example, a recent study co-cultured ECs and fibroblasts in a vessel-on-a-chip model of microvasculature and showed that a stiffness of 20 kPa reduced vessel area and promoted PMT, as quantified by the expression of collagen 1 and  $\alpha$ SMA (45). Further, studies analyzing IPF samples report that mature scar is completely void of microvessels (78–80), which is consistent with the extreme reduction in microvessel area in mature fibrosis (20 kPa) that was predicted by our model and validated by our experiments. Hence,

our model predictions and experiments contribute to the published literature by suggesting that ECM stiffness drives EC-pericyte uncoupling, leading to EC apoptosis and pericyte PMT, and causing microvascular regression.

Since nintedanib is a standard of care treatment for IPF (26), it is important to understand how the cell state changes evoked by this drug scale-up to impact microvessel remodeling. At the intracellular level, our mechanistic sub-network analysis identified several pathways that were pertinent to how nintedanib functions inside ECs and pericytes. Of particular interest was the result that the PI3 K pathway regulated quiescence in both ECs and pericytes, as a recent study in the bleomycin mouse model found that nintedanib ameliorated inflammation and fibrosis specifically through the PI3 K pathway (82). This supports the role of nintedanib in controlling cell fate through the PI3 K pathway; however, our model predicted that it negatively impacts EC-pericyte coupling. Specifically, the multiscale model predicted that nintedanib disrupts the ability for EC-pericyte recoupling after an initial decrease in the percent of quiescent pericytes, potentiating PMT in environments with higher ECM stiffnesses. This prediction is important because decreases in the percentage of quiescent pericytes, even when 95% of ECs (or more) are able to return to a quiescent state, could cause excessive vascular leakage, an outcome of defective microvessel remodeling that has been reported in IPF patients (28, 29). Excessive vascular leakage, particularly that which causes alveolar edema, can also be detrimental to gas exchange and lead to poor outcomes (29, 83).

At the tissue level, nintedanib reduced vessel area in both the soft (2 kPa) and immature fibrotic (10 kPa) environments of our experimental model, which was consistent with our multiscale model's predictions of vessel regression in response to nintedanib in these environments. This adds to existing literature that has demonstrated nintedanib's antiproliferative effects in ECs and pericytes (84, 85), as well as inhibition of EC-mural cell coupling (77). Importantly, IPF is a progressive disease in which the lung becomes increasingly stiff over time, characterized by significant spatial heterogeneity in fibrotic foci distribution and gene expression (86). This suggests that the effects of currently available antifibrotic treatments vary, both temporally within an individual over time and spatially across the lung.

Finally, we used our model to determine if targeting a specific node in the intracellular signaling network of pericytes would prevent nintedanib-induced PMT, restore EC-pericyte coupling, and increase microvessel homeostasis. YAP/TAZ-mediated signaling was identified by our model sensitivity analysis as a key regulator of pericyte migration and PMT and has previously been studied as a target for preventing fibrosis (87, 88). Simulating dual treatment with nintedanib and YAP/TAZ inhibition at 10 kPa improved both cell- and tissue-level outcomes. However, the benefits of inhibiting YAP/TAZ signaling were partially negated by an ECM stiffness of 20 kPa. Interestingly, YAP/TAZ inhibitors have been suggested to have potential benefits in IPF by mitigating fibroblast activation (87, 88).

Multiscale computational modeling offers a unique framework for integrating data sets across cell, tissue, and organ-level contexts. In the present study we combine logic-based network modeling, which captures dynamically complex intracellular signaling networks and pharmacological responses at the single-cell level, with an ABM that provides a multicell, spatial, and stochastic framework (89). This framework enables us to draw novel conclusions about the consequences of individual cell behaviors and phenotype changes on the dynamic, structural remodeling of tissues. Others have previously used ABMs to explore the

mechanisms of disease progression in many conditions, including lung infections (90–94), fibrosis (2, 50–53, 95), skeletal muscle regeneration (47, 96–98), and cancer (99–102). Our group has previously used ABM to study mechanisms of angiogenesis and vascular remodeling (46, 49, 103, 104). For example, Walpole et al. developed an ABM of retinal angiogenesis in which ECs migrate along a network of VEGF-secreting astrocytes to form new sprouts in the presence or absence of pericytes. Incorporation of pericytes in the model significantly improved the accuracy of the model's prediction of microvascular remodeling, when experimentally validated against retinas from post-natal day 3 mice. While that model did not explicitly simulate intracellular signaling, it highlighted the importance of including both ECs and pericytes in computational models of microvascular remodeling, as their interactions are key regulators of this process. Our multiscale model, which incorporates intracellular signaling in both cell types, extends the model by Walpole et al., by suggesting differential phenotypic responses by simulated ECs and pericytes to the same biomechanical and biochemical cues. This further underscores the importance of including both pericytes and ECs in models of microvascular remodeling and simulating not only their interactions with one another, but also their unique responses to the microenvironment which are interpreted by intracellular signaling networks that are unique to each cell type. Given that logic-based ordinary differential equations modeling has been used to represent many different cell types, including ECs (55), smooth muscle cells (105), fibroblasts (56, 106–110), and cardiomyocytes (57, 111–113), our multiscale computational model can be extended to study other cell or tissue phenotypes by integrating new and previously established intracellular signaling models. Multiscale models overall have become more popular in recent years for their advantages in integrating multiscale data and producing novel understanding of disease progression at different biological scales, as has been reviewed in several recent papers (1, 114–118).

There are several limitations to our experimental studies and to our multiscale computational model. Given that the presentation of IPF varies across patients and across different regions of the lung of the same patient, the effects of nintedanib are also likely to be variable. While our findings align with prior studies, we simulated only a limited number of initial conditions and environmental stiffnesses, but our model could be refined through additional data-driven parametrization to represent individual patients or lung regions. A limitation of our experimental explant model is the use of healthy mouse lung tissue, which may not exhibit the same phenotypic responses as diseased human lung. Despite this limitation, the experimental system provided a reproducible way to determine how ECM stiffness affects microvessel remodeling. The computational model only included ECs and pericytes; however, there are many cells in this interstitial niche, including epithelial cells, fibroblasts, and immune cells. Future versions of this model can incorporate epithelial cells to better capture the capillary-alveolar interface or fibroblasts, which contribute to the progressive stiffening of the matrix in IPF (1, 119–122). Additionally, the model simulated only a small portion of lung (500  $\mu\text{m}$   $\times$  500  $\mu\text{m}$ ) over a short time period of 1 week. The simulation size was largely limited by the number of cells, as more cells increased the overall time to compute. Additionally, the signaling pathways included in the EC and pericyte network models were limited to those that were deemed essential to represent EC-pericyte coupling and cell fate decisions. While it is likely that other signaling pathways are also important, and the current pathways in the models could be represented in more

detail by including additional nodes, and these adaptations can be included in future model iterations. One example is the addition of more detailed pathways that respond to mechanical signaling, such as TGF $\beta$  activation by mechanical stiffness. The integration of these models with artificial intelligence and machine learning models can potentiate these advancements if provided with enough mechanistic biological data to train the models (123). Moreover, the independent validation we performed by comparing predictions to published literature suggested that the pathways that were included in the current version of the models were sufficient to invoke the major phenotypic states of ECs and pericytes. That being said, our review of the literature also revealed holes that can be filled by future studies, specifically in the quantification of microvascular remodeling in IPF patients. Lastly, while NetLogo provided advantages as an ABM software one major limitation is the discrete square lattice on which the model is built limiting spatial resolution.

Future studies should prioritize adapting the multiscale model to patient-specific contexts. For example, here we begin with an IF image of healthy lung vasculature to account for EC–pericyte ratios and a general vascular network starting point; but this can be replaced with other images in which specific EC and pericyte locations can be identified. Additionally, growth factors are known to be highly dysregulated in IPF, with evidence of extremely low VEGF availability (40), increased abundance of PDGF (38), and a decrease in Ang1 associated with an increase in its agonist ligand, Ang2 (36). Read outs of these protein levels as serum biomarkers could allow for patient-specific modeling. Moreover, incorporation of the other FDA approved drug for IPF, pirfenidone, a small molecule inhibitor of TGF $\beta$ , would also be of interest, as TGF $\beta$  regulates both proangiogenic and proquiescent pathways in ECs and proquiescent and profibrotic pathways in pericytes (124, 125). Additionally, we assumed that tissue stiffness levels remained constant, which resulted in a transient drop in EC quiescence as cells adjusted to the changes in stiffness. However, future simulations should represent the progressive stiffening that occurs in IPF. ABMs have been used by others to study progressive stiffening of the ECM in IPF by representing the ECM as a network of springs that is remodeled overtime by fibroblasts (50, 51, 126). Lastly, other potential pathways for preserving EC–pericyte coupling can be explored to identify novel therapies and combination therapies to maintain microvessel homeostasis in IPF.

In conclusion, we have developed a multiscale modeling framework that integrates dynamically complex intracellular signaling networks in different cell types with cell–cell and cell–environment communication to elucidate mechanisms underpinning the loss of microvascular homeostasis in the context of IPF. This work highlights the need for more research on vascular remodeling in IPF and the benefits of combining computational and experimental models to study interacting heterogeneous cell populations in spatially complex, remodeling microenvironments.

## Methods

Details of all methods are described in the [Supplementary material](#).

## Acknowledgments

The authors would like to thank Riley Hannan, Ph.D. for his assistance with collecting the IF image used in the ABM setup.

## Supplementary Material

[Supplementary material](#) is available at PNAS Nexus online.

## Funding

This work was supported in part by the National Institutes of Health (R01HL155143 to S.M.P. and T.H.B., R01GM140008 to S.M.P., and T32 HL007284 to J.L.D.), the National Science Foundation (NSF-20211130 ISSNL and NSF-BMMB 2140549 to S.M.P.).

## Author Contributions

Figure and manuscript preparation: J.L.D., S.M.J.A., D.J.C., L.J.T., and S.M.P. Conceptualization: J.L.D., T.H.B., C.A., J.J.S., L.J.T., and S.M.P. Study design: J.L.D. and S.M.P. Data collection: J.L.D., S.M.J.A., D.J.C., T.N.T., and A.C.B. Data analysis: J.L.D., S.M.J.A., D.J.C., T.G.E. and T. C. All authors participated in the review and approval of the final manuscript.

## Preprints

This manuscript was posted on a preprint: <https://doi.org/10.1101/2024.03.15.585249>

## Data Availability

All data are included in the manuscript and supporting information. Netflux model information is included in the [Supplementary material](#). Multiscale model code is available on GitHub at <https://github.com/Peirce-Cotter-Lab/Leonard-Duke-et-al.-2024—PNAS-Nexus>.

## References

- Leonard-Duke J, et al. 2020. Multi-scale models of lung fibrosis. *Matrix Biol.* 91–92:35–50.
- Rikard SM, et al. 2019. Multiscale coupling of an agent-based model of tissue fibrosis and a logic-based model of intracellular signaling. *Front Physiol.* 10:1481.
- Jain RK. 2003. Molecular regulation of vessel maturation. *Nat Med.* 9(6):685–693.
- Zeng H, et al. 2016. LPS causes pericyte loss and microvascular dysfunction via disruption of Sirt3/angiopoietins/Tie-2 and HIF-2 $\alpha$ /Notch3 pathways. *Sci Rep.* 6(1):20931.
- Bergers G, Song S. 2005. The role of pericytes in blood-vessel formation and maintenance. *Neuro Oncol.* 7(4):452–464.
- Dibble M, Di Cio' S, Luo P, Balkwill F, Gautrot JE. 2023. The impact of pericytes on the stability of microvascular networks in response to nanoparticles. *Sci Rep.* 13(1):5729.
- Armulik A, Abramsson A, Betsholtz C. 2005. Endothelial/pericyte interactions. *Circ Res.* 97(6):512–523.
- Dabravolski SA, et al. 2023. The role of pericytes in regulation of innate and adaptive immunity. *Biomedicines.* 11(2):600.
- Török O, et al. 2021. Pericytes regulate vascular immune homeostasis in the CNS. *Proc Natl Acad Sci U S A.* 118(10):e2016587118.
- Niu F, et al. 2019. Cocaine-induced release of CXCL10 from pericytes regulates monocyte transmigration into the CNS. *J Cell Biol.* 218(2):700–721.
- Maier CL, Poher JS. 2011. Human placental pericytes poorly stimulate and actively regulate allogeneic CD4 T cell responses. *Arterioscler Thromb Vasc Biol.* 31(1):183–189.

- 12 Tu Z, et al. 2011. Retinal pericytes inhibit activated T cell proliferation. *Invest Ophthalmol Vis Sci.* 52(12):9005–9010.
- 13 Sava P, Cook IO, Mahal RS, Gonzalez AL. 2015. Human microvascular pericyte basement membrane remodeling regulates neutrophil recruitment. *Microcirculation.* 22(1):54–67.
- 14 Rayner SG, Hung CF, Liles WC, Altemeier WA. 2023. Lung pericytes as mediators of inflammation. *Am J Physiol Lung Cell Mol Physiol.* 325(1):L1–L8.
- 15 Choe Y-G, et al. 2022. Pericyte loss leads to capillary stalling through increased leukocyte-endothelial cell interaction in the brain. *Front Cell Neurosci.* 16:848764.
- 16 Hartmann DA, Coelho-Santos V, Shih AY. 2022. Pericyte control of blood flow across microvascular zones in the central nervous system. *Annu Rev Physiol.* 84(1):331–354.
- 17 Hamilton N, Attwell D, Hall C. 2010. Pericyte-mediated regulation of capillary diameter: a component of neurovascular coupling in health and disease. *Front Neuroenergetics.* 2:5.
- 18 Mammoto A, Mammoto T. 2019. Vascular niche in lung alveolar development, homeostasis, and regeneration. *Front Bioeng Biotechnol.* 7:318.
- 19 Caporarello N, et al. 2020. Vascular dysfunction in aged mice contributes to persistent lung fibrosis. *Aging Cell.* 19(8):e13196.
- 20 Caporarello N, Ligresti G. 2023. Vascular contribution to lung repair and fibrosis. *Am J Respir Cell Mol Biol.* 69(2):135–146.
- 21 Gerhardt H, Betsholtz C. 2003. Endothelial-pericyte interactions in angiogenesis. *Cell Tissue Res.* 314(1):15–23.
- 22 Plantier L, et al. 2018. Physiology of the lung in idiopathic pulmonary fibrosis. *Eur Respir Rev.* 27(147):170062.
- 23 Ley B, Collard HR. 2013. Epidemiology of idiopathic pulmonary fibrosis. *Clin Epidemiol.* 5:483–492.
- 24 Ley B, Collard HR, King TE Jr. 2011. Clinical course and prediction of survival in idiopathic pulmonary fibrosis. *Am J Respir Crit Care Med.* 183(4):431–440.
- 25 Maher TM. 2013. PROFILEing idiopathic pulmonary fibrosis: rethinking biomarker discovery. *Eur Respir Rev.* 22(128):148–152.
- 26 Raghu G, et al. 2022. Idiopathic pulmonary fibrosis (an update) and progressive pulmonary fibrosis in adults: an official ATS/ERS/JRS/ALAT clinical practice guideline. *Am J Respir Crit Care Med.* 205(9):e18–e47.
- 27 Sauleda J, Núñez B, Sala E, Soriano JB. 2018. Idiopathic pulmonary fibrosis: epidemiology, natural history, phenotypes. *Med Sci (Basel).* 6(4):110.
- 28 Montesi SB, et al. 2018. Gadofosveset-enhanced lung magnetic resonance imaging to detect ongoing vascular leak in pulmonary fibrosis. *Eur Respir J.* 51(5):1800171.
- 29 Probst CK, Montesi SB, Medoff BD, Shea BS, Knipe RS. 2020. Vascular permeability in the fibrotic lung. *Eur Respir J.* 56(1):1900100.
- 30 Renzoni EA. 2004. Neovascularization in idiopathic pulmonary fibrosis: too much or too little? *Am J Respir Crit Care Med.* 169(11):1179–1180.
- 31 Hanumegowda C, Farkas L, Kolb M. 2012. Angiogenesis in pulmonary fibrosis: too much or not enough? *Chest.* 142(1):200–207.
- 32 Hannan RT, et al. 2021. Extracellular matrix remodeling associated with bleomycin-induced lung injury supports pericyte-to-myofibroblast transition. *Matrix Biol Plus.* 10:100056.
- 33 Sava P, et al. 2017. Human pericytes adopt myofibroblast properties in the microenvironment of the IPF lung. *JCI Insight.* 2(24):e96352.
- 34 Uehara M, et al. 2016. Impact of angiotensin-1 and -2 on clinical course of idiopathic pulmonary fibrosis. *Respir Med.* 114:18–26.
- 35 Ando M, et al. 2016. Angiotensin-2 expression in patients with an acute exacerbation of idiopathic interstitial pneumonias. *Respir Med.* 117:27–32.
- 36 Margaritopoulos GA, et al. 2010. Investigation of angiogenic axis angiotensin-1 and -2/Tie-2 in fibrotic lung diseases: a bronchoalveolar lavage study. *Int J Mol Med.* 26(6):919–923.
- 37 Antoniadis HN, et al. 1990. Platelet-derived growth factor in idiopathic pulmonary fibrosis. *J Clin Invest.* 86(4):1055–1064.
- 38 Martinet Y, Rom WN, Grotendorst GR, Martin GR, Crystal RG. 1987. Exaggerated spontaneous release of platelet-derived growth factor by alveolar macrophages from patients with idiopathic pulmonary fibrosis. *N Engl J Med.* 317(4):202–209.
- 39 Cao B, Guo Z, Zhu Y, Xu W. 2000. The potential role of PDGF, IGF-1, TGF-beta expression in idiopathic pulmonary fibrosis. *Chin Med J (Engl).* 113(09):776–782.
- 40 Murray LA, et al. 2017. Antifibrotic role of vascular endothelial growth factor in pulmonary fibrosis. *JCI Insight.* 2(16):e92192.
- 41 Liu X, et al. 2023. Multiple fibroblast subtypes contribute to matrix deposition in pulmonary fibrosis. *Am J Respir Cell Mol Biol.* 69(1):45–56.
- 42 Wollin L, et al. 2015. Mode of action of nintedanib in the treatment of idiopathic pulmonary fibrosis. *Eur Respir J.* 45(5):1434.
- 43 Hosaka K, et al. 2018. Dual roles of endothelial FGF-2-FGFR1-PDGF-BB and perivascular FGF-2-FGFR2-PDGF $\beta$  signaling pathways in tumor vascular remodeling. *Cell Discov.* 4(1):3.
- 44 Fiore VF, et al. 2018.  $\alpha$ v $\beta$ 3 Integrin drives fibroblast contraction and strain stiffening of soft provisional matrix during progressive fibrosis. *JCI Insight.* 3(20):e97597.
- 45 Yu Y, et al. 2023. Extracellular matrix stiffness regulates microvascular stability by controlling endothelial paracrine signaling to determine pericyte fate. *Arterioscler Thromb Vasc Biol.* 43(10):1887–1899.
- 46 Walpole J, Mac Gabhann F, Peirce SM, Chappell JC. 2017. Agent-based computational model of retinal angiogenesis simulates microvascular network morphology as a function of pericyte coverage. *Microcirculation.* 24(8):e12393.
- 47 Virgilio KM, Martin KS, Peirce SM, Blemker SS. 2018. Agent-based model illustrates the role of the microenvironment in regeneration in healthy and mdx skeletal muscle. *J Appl Physiol* (1985). 125(5):1424–1439.
- 48 Walpole J, et al. 2015. Agent-based model of angiogenesis simulates capillary sprout initiation in multicellular networks. *Integr Biol (Camb).* 7(9):987–997.
- 49 Peirce SM, Van Gieson EJ, Skalak TC. 2004. Multicellular simulation predicts microvascular patterning and in silico tissue assembly. *FASEB J.* 18(6):731–733.
- 50 Hall JK, et al. 2024. Elucidating the interaction between stretch and stiffness using an agent-based spring network model of progressive pulmonary fibrosis. *Front Netw Physiol.* 4:1396383.
- 51 Wellman TJ, Mondoñedo JR, Davis GS, Bates JH, Suki B. 2018. Topographic distribution of idiopathic pulmonary fibrosis: a hybrid physics-and agent-based model. *Physiol Meas.* 39(6):064007.
- 52 Islam MA, Getz M, Macklin P, Ford Versypt AN. 2023. An agent-based modeling approach for lung fibrosis in response to COVID-19. *PLoS Comput Biol.* 19(12):e1011741.
- 53 Shen Y, Feng F, Sun H, Li G, Xiang Z. 2020. Quantitative and network pharmacology: a case study of rhein alleviating pathological progress of renal interstitial fibrosis. *J Ethnopharmacol.* 261:113106.
- 54 Kraeutler MJ, Soltis AR, Saucerman JJ. 2010. Modeling cardiac  $\beta$ -adrenergic signaling with normalized-Hill differential equations: comparison with a biochemical model. *BMC Syst Biol.* 4(1):157.

- 55 Gorick CM, Saucerman JJ, Price RJ. 2022. Computational model of brain endothelial cell signaling pathways predicts therapeutic targets for cerebral pathologies. *J Mol Cell Cardiol.* 164:17–28.
- 56 Zeigler AC, Richardson WJ, Holmes JW, Saucerman JJ. 2016. A computational model of cardiac fibroblast signaling predicts context-dependent drivers of myofibroblast differentiation. *J Mol Cell Cardiol.* 94:72–81.
- 57 Eggertsen TG, Saucerman JJ. 2023. Virtual drug screen reveals context-dependent inhibition of cardiomyocyte hypertrophy. *Br J Pharmacol.* 180(21):2721–2735.
- 58 NetLogo. 1999. *Center for connected learning and computer-based modeling* Evanston (IL): Northwestern University.
- 59 Hori Y, et al. 2017. Functional characterization of VEGF- and FGF-induced tumor blood vessel models in human cancer xenografts. *Anticancer Res.* 37(12):6629–6638.
- 60 Nör JE, Christensen J, Mooney DJ, Polverini PJ. 1999. Vascular endothelial growth factor (VEGF)-mediated angiogenesis is associated with enhanced endothelial cell survival and induction of bcl-2 expression. *Am J Pathol.* 154(2):375–384.
- 61 Franco M, Roswall P, Cortez E, Hanahan D, Pietras K. 2011. Pericytes promote endothelial cell survival through induction of autocrine VEGF-A signaling and Bcl-w expression. *Blood.* 118(10):2906–2917.
- 62 LaBarbera KE, Hyldahl RD, O'Fallon KS, Clarkson PM, Witkowski S. 2015. Pericyte NF- $\kappa$ B activation enhances endothelial cell proliferation and proangiogenic cytokine secretion in vitro. *Physiol Rep.* 3(4):e12309.
- 63 Viñals F, Pouyssegur J. 2001. Transforming growth factor  $\beta$ 1 (TGF- $\beta$ 1) promotes endothelial cell survival during in vitro angiogenesis via an autocrine mechanism implicating TGF- $\alpha$  signaling. *Mol Cell Biol.* 21(21):7218–7230.
- 64 Rostama B, et al. 2015. DLL4/Notch1 and BMP9 interdependent signaling induces human endothelial cell quiescence via P27KIP1 and thrombospondin-1. *Arterioscler Thromb Vasc Biol.* 35(12):2626–2637.
- 65 Hou Z, et al. 2018. Platelet-derived growth factor subunit B signaling promotes pericyte migration in response to loud sound in the cochlear stria vascularis. *J Assoc Res Otolaryngol.* 19(4):363–379.
- 66 Abramsson A, Lindblom P, Betsholtz C. 2003. Endothelial and nonendothelial sources of PDGF-B regulate pericyte recruitment and influence vascular pattern formation in tumors. *J Clin Invest.* 112(8):1142–1151.
- 67 Liu H, Kennard S, Lilly B. 2009. NOTCH3 expression is induced in mural cells through an autoregulatory loop that requires endothelial-expressed JAGGED1. *Circ Res.* 104(4):466–475.
- 68 Ji Y, et al. 2016. Jagged1/Notch3 signaling modulates hemangioma-derived pericyte proliferation and maturation. *Cell Physiol Biochem.* 40(5):895–907.
- 69 Feng F, Feng X, Zhang D, Li Q, Yao L. 2021. Matrix stiffness induces pericyte-fibroblast transition through YAP activation. *Front Pharmacol.* 12:698275.
- 70 Yamaguchi M, et al. 2020. Pericyte-myofibroblast transition in the human lung. *Biochem Biophys Res Commun.* 528(2):269–275.
- 71 Zhao Z, et al. 2022. TGF- $\beta$  promotes pericyte-myofibroblast transition in subretinal fibrosis through the Smad2/3 and Akt/mTOR pathways. *Exp Mol Med.* 54(5):673–684.
- 72 Stratman AN, Schwindt AE, Malotte KM, Davis GE. 2010. Endothelial-derived PDGF-BB and HB-EGF coordinately regulate pericyte recruitment during vasculogenic tube assembly and stabilization. *Blood.* 116(22):4720–4730.
- 73 Hall AP, et al. 2015. PDGFR inhibition results in pericyte depletion and hemorrhage into the Corpus Luteum of the rat ovary. *Toxicol Pathol.* 44(1):98–111.
- 74 Tammela T, Enholm B, Alitalo K, Paavonen K. 2005. The biology of vascular endothelial growth factors. *Cardiovasc Res.* 65(3):550–563.
- 75 Gavalas NG, et al. 2013. Angiogenesis-related pathways in the pathogenesis of ovarian cancer. *Int J Mol Sci.* 14(8):15885–15909.
- 76 Leonard-Duke J, Bruce AC, Peirce SM, Taite LJ. 2023. Variations in mechanical stiffness alter microvascular sprouting and stability in a PEG hydrogel model of idiopathic pulmonary fibrosis. *Microcirculation.* 30(5–6):e12817.
- 77 Zeinali S, et al. 2018. Human microvasculature-on-a chip: anti-neovascularogenic effect of nintedanib in vitro. *Angiogenesis.* 21(4):861–871.
- 78 Ebina M, et al. 2004. Heterogeneous increase in CD34-positive alveolar capillaries in idiopathic pulmonary fibrosis. *Am J Respir Crit Care Med.* 169(11):1203–1208.
- 79 Keane MP, et al. 1997. The CXC chemokines, IL-8 and IP-10, regulate angiogenic activity in idiopathic pulmonary fibrosis. *J Immunol.* 159(3):1437–1443.
- 80 Keane MP, et al. 1999. Neutralization of the CXC chemokine, macrophage inflammatory protein-2, attenuates bleomycin-induced pulmonary fibrosis. *J Immunol.* 162(9):5511–5518.
- 81 Ackermann M, et al. 2017. Effects of nintedanib on the microvascular architecture in a lung fibrosis model. *Angiogenesis.* 20(3):359–372.
- 82 Pan L, et al. 2023. Nintedanib ameliorates bleomycin-induced pulmonary fibrosis, inflammation, apoptosis, and oxidative stress by modulating PI3K/akt/mTOR pathway in mice. *Inflammation.* 46(4):1531–1542.
- 83 Bull TM, Clark B, McFann K, Moss M. 2010. Pulmonary vascular dysfunction is associated with poor outcomes in patients with acute lung injury. *Am J Respir Crit Care Med.* 182(9):1123–1128.
- 84 Hilberg F, et al. 2008. BIBF 1120: triple angiokinase inhibitor with sustained receptor blockade and good antitumor efficacy. *Cancer Res.* 68(12):4774–4782.
- 85 Rol N, et al. 2019. Nintedanib improves cardiac fibrosis but leaves pulmonary vascular remodelling unaltered in experimental pulmonary hypertension. *Cardiovasc Res.* 115(2):432–439.
- 86 Huang Y, et al. 2023. Central lung gene expression associates with myofibroblast features in idiopathic pulmonary fibrosis. *BMJ Open Respir Res.* 10(1):e001391.
- 87 Yang Y, et al. 2022. Screening for inhibitors of YAP nuclear localization identifies aurora kinase A as a modulator of lung fibrosis. *Am J Respir Cell Mol Biol.* 67(1):36–49.
- 88 Haak AJ, et al. 2019. Selective YAP/TAZ inhibition in fibroblasts via dopamine receptor D1 agonism reverses fibrosis. *Sci Transl Med.* 11(516):eaau6296.
- 89 Walpole J, Papin JA, Peirce SM. 2013. Multiscale computational models of complex biological systems. *Annu Rev Biomed Eng.* 15:137–154.
- 90 Weathered C, Pennington K, Escalante P, Pienaar E. 2023. Agent-based model indicates chemoattractant signaling caused by *Mycobacterium avium* biofilms in the lung airway increases bacterial loads by spatially diverting macrophages. *Tuberculosis.* 138:102300.
- 91 Budak M, et al. 2023. Optimizing tuberculosis treatment efficacy: comparing the standard regimen with Moxifloxacin-containing regimens. *PLoS Comput Biol.* 19(6):e1010823.
- 92 Warsinske HC, Pienaar E, Linderman JJ, Mattila JT, Kirschner DE. 2017. Deletion of TGF- $\beta$ 1 increases bacterial clearance by cytotoxic T cells in a tuberculosis granuloma model. *Front Immunol.* 8:1843.
- 93 Oremland M, et al. 2016. A computational model of invasive aspergillosis in the lung and the role of iron. *BMC Syst Biol.* 10(1):34.

- 94 Ribeiro HA, et al. 2022. Multi-scale mechanistic modelling of the host defence in invasive aspergillosis reveals leucocyte activation and iron acquisition as drivers of infection outcome. *J R Soc Interface*. 19(189):20210806.
- 95 Warsinske HC, DiFazio RM, Linderman JJ, Flynn JL, Kirschner DE. 2017. Identifying mechanisms driving formation of granuloma-associated fibrosis during *Mycobacterium tuberculosis* infection. *J Theor Biol*. 429:1–17.
- 96 Haase M, Comlekoglu T, Petruccianni A, Peirce SM, Blemker SS. 2024. *Agent-based model demonstrates the impact of nonlinear, complex interactions between cytokines on muscle regeneration* eLife Sciences Publications, Ltd.
- 97 Martin KS, et al. 2017. In silico and in vivo experiments reveal M-CSF injections accelerate regeneration following muscle laceration. *Ann Biomed Eng*. 45(3):747–760.
- 98 Virgilio KM, et al. 2021. Computational models provide insight into in vivo studies and reveal the complex role of fibrosis in mdx muscle regeneration. *Ann Biomed Eng*. 49(2):536–547.
- 99 Cess CG, Finley SD. 2022. Multiscale modeling of tumor adaptation and invasion following anti-angiogenic therapy. *Comput Syst Oncol*. 2(1):e1032.
- 100 Poleszczuk J, Macklin P, Enderling H. 2016. Agent-based modeling of cancer stem cell driven solid tumor growth. *Methods Mol Biol*. 1516:335–346.
- 101 Gong C, et al. 2017. A computational multiscale agent-based model for simulating spatio-temporal tumour immune response to PD1 and PDL1 inhibition. *J R Soc Interface*. 14(134):20170320.
- 102 Norton K-A, Wallace T, Pandey NB, Popel AS. 2017. An agent-based model of triple-negative breast cancer: the interplay between chemokine receptor CCR5 expression, cancer stem cells, and hypoxia. *BMC Syst Biol*. 11(1):68.
- 103 Alhashem Z, et al. 2022. Notch controls the cell cycle to define leader versus follower identities during collective cell migration. *eLife*. 11:e73550.
- 104 Keshavarzian M, Meyer CA, Hayenga HN. 2018. Mechanobiological model of arterial growth and remodeling. *Biomech Model Mechanobiol*. 17(1):87–101.
- 105 Estrada AC, et al. 2021. Roles of mTOR in thoracic aortopathy understood by complex intracellular signaling interactions. *PLoS Comput Biol*. 17(12):e1009683.
- 106 Rogers JD, Aguado BA, Watts KM, Anseth KS, Richardson WJ. 2022. Network modeling predicts personalized gene expression and drug responses in valve myofibroblasts cultured with patient sera. *Proc Natl Acad Sci U S A*. 119(8):e2117323119.
- 107 Zeigler AC, et al. 2021. Network model-based screen for FDA-approved drugs affecting cardiac fibrosis. *CPT Pharmacometrics Syst Pharmacol*. 10(4):377–388.
- 108 Nelson AR, Bugg D, Davis J, Saucerman JJ. 2023. Network model integrated with multi-omic data predicts MBNL1 signals that drive myofibroblast activation. *iScience*. 26(4):106502.
- 109 Wang A, Cao S, Aboelkassem Y, Valdez-Jasso D. 2020. Quantification of uncertainty in a new network model of pulmonary arterial adventitial fibroblast pro-fibrotic signalling. *Philos Trans A Math Phys Eng Sci*. 378(2173):20190338.
- 110 Nelson AR, Christiansen SL, Naegle KM, Saucerman JJ. 2024. Logic-based mechanistic machine learning on high-content images reveals how drugs differentially regulate cardiac fibroblasts. *Proc Natl Acad Sci U S A*. 121(5):e2303513121.
- 111 Khalilimeybodi A, et al. 2023. Signaling network model of cardiomyocyte morphological changes in familial cardiomyopathy. *J Mol Cell Cardiol*. 174:1–14.
- 112 Tan PM, Buchholz KS, Omens JH, McCulloch AD, Saucerman JJ. 2017. Predictive model identifies key network regulators of cardiomyocyte mechano-signaling. *PLoS Comput Biol*. 13(11):e1005854.
- 113 Cao S, et al. 2020. Quantification of model and data uncertainty in a network analysis of cardiac myocyte mechanosignalling. *Philos Trans A Math Phys Eng Sci*. 378(2173):20190336.
- 114 Ford Versypt AN. 2021. Multiscale modeling in disease. *Curr Opin Syst Biol*. 27:100340.
- 115 Warner HV, Sivakumar N, Peirce SM, Lazzara MJ. 2019. Multiscale computational models of cancer. *Curr Opin Biomed Eng*. 11:137–144.
- 116 Layton AT. 2019. Multiscale models of kidney function and diseases. *Curr Opin Biomed Eng*. 11:1–8.
- 117 Cappuccio A, Tieri P, Castiglione F. 2016. Multiscale modelling in immunology: a review. *Brief Bioinform*. 17(3):408–418.
- 118 Talman L, Agmon E, Peirce SM, Covert MW. 2019. Multiscale models of infection. *Curr Opin Biomed Eng*. 11:102–108.
- 119 Hannan RT, Peirce SM, Barker TH. 2018. Fibroblasts: diverse cells critical to biomaterials integration. *ACS Biomater Sci Eng*. 4(4):1223–1232.
- 120 Yu G, Ibarra GH, Kaminski N. 2018. Fibrosis: lessons from OMICS analyses of the human lung. *Matrix Biol*. 68–69:422–434.
- 121 White ES. 2015. Lung extracellular matrix and fibroblast function. *Ann Am Thorac Soc*. 12 Suppl 1:S30–S33.
- 122 Camelo A, Dunmore R, Sleeman MA, Clarke DL. 2014. The epithelium in idiopathic pulmonary fibrosis: breaking the barrier. *Front Pharmacol*. 4:173.
- 123 Sivakumar N, Mura C, Peirce SM. 2022. Innovations in integrating machine learning and agent-based modeling of biomedical systems. *Front Syst Biol*. 2. <https://doi.org/10.3389/fsysb.2022.959665>
- 124 Goumans M-J, Liu Z, ten Dijke P. 2009. TGF- $\beta$  signaling in vascular biology and dysfunction. *Cell Res*. 19(1):116–127.
- 125 Sweeney MD, Ayyadurai S, Zlokovic BV. 2016. Pericytes of the neurovascular unit: key functions and signaling pathways. *Nat Neurosci*. 19(6):771–783.
- 126 Oliveira CL, Bates JH, Suki B. 2014. A network model of correlated growth of tissue stiffening in pulmonary fibrosis. *New J Phys*. 16(6):065022.
- 127 Shannon P, et al. 2003. Cytoscape: a software environment for integrated models of biomolecular interaction networks. *Genome Res*. 13(11):2498–2504.
- 128 Hillen F, Griffioen AW. 2007. Tumour vascularization: sprouting angiogenesis and beyond. *Cancer Metastasis Rev*. 26(3):489–502.
- 129 Hayenga HN, Thorne BC, Peirce SM, Humphrey JD. 2011. Ensuring congruency in multiscale modeling: towards linking agent based and Continuum biomechanical models of arterial adaptation. *Ann Biomed Eng*. 39(11):2669.
- 130 McManus LM, Mitchell RN. *Pathobiology of human disease: a dynamic encyclopedia of disease mechanisms*, Elsevier, 2014.
- 131 Kato K, et al. 2018. Pulmonary pericytes regulate lung morphogenesis. *Nat Commun*. 9(1):2448.
- 132 Su H, Cantrell AC, Zeng H, Zhu SH, Chen JX. 2021. Emerging role of pericytes and their secretome in the heart. *Cells*. 10(3):548.
- 133 Hellström M, et al. 2007. Dll4 signalling through notch1 regulates formation of tip cells during angiogenesis. *Nature*. 445(7129):776–780.
- 134 Chappell JC, Wiley DM, Bautch VL. 2011. Regulation of blood vessel sprouting. *Semin Cell Dev Biol*. 22(9):1005–1011.
- 135 Nwadozi E, Rudnicki M, Haas TL. 2020. Metabolic coordination of pericyte phenotypes: therapeutic implications. *Front Cell Dev Biol*. 8:77.

- 136 Corliss BA, et al. 2020. Pericyte bridges in homeostasis and hyperglycemia. *Diabetes*. 69(7):1503–1517.
- 137 Corliss BA, et al. 2019. Myh11 lineage corneal endothelial cells and ASCs populate corneal endothelium. *Invest Ophthalmol Vis Sci*. 60(15):5095–5103.
- 138 Schweller RM, West JL. 2015. Encoding hydrogel mechanics via network cross-linking structure. *ACS Biomater Sci Eng*. 1(5):335–344.
- 139 Gill BJ, et al. 2012. A synthetic matrix with independently tunable biochemistry and mechanical properties to study epithelial morphogenesis and EMT in a lung adenocarcinoma model. *Cancer Res*. 72(22):6013–6023.
- 140 Chapla R, Alhaj Abed M, West J. 2020. Modulating functionalized poly(ethylene glycol) diacrylate hydrogel mechanical properties through competitive crosslinking mechanics for soft tissue applications. *Polymers (Basel)*. 12(12):3000.
- 141 Wakefield LM, Smith DM, Masui T, Harris CC, Sporn MB. 1987. Distribution and modulation of the cellular receptor for transforming growth factor-beta. *J Cell Biol*. 105(2):965–975.
- 142 Chlebova K, et al. 2009. High molecular weight FGF2: the biology of a nuclear growth factor. *Cell Mol Life Sci*. 66(2):225–235.
- 143 Ibrahimi OA, Zhang F, Lang Hrstka SC, Mohammadi M, Linhardt RJ. 2004. Kinetic model for FGF, FGFR, and proteoglycan signal transduction complex assembly. *Biochemistry*. 43(16):4724–4730.
- 144 Gabhann M, Popel F, S A. 2007. Dimerization of VEGF receptors and implications for signal transduction: a computational study. *Biophys Chem*. 128(2–3):125–139.
- 145 Oates TW, et al. 1995. Receptor binding of PDGF-AA and PDGF-BB, and the modulation of PDGF receptors by TGF-beta, in human periodontal ligament cells. *J Cell Physiol*. 162(3):359–366.
- 146 Gerhardt H, Wolburg H, Redies C. 2000. N-cadherin mediates pericytic-endothelial interaction during brain angiogenesis in the chicken. *Dev Dyn*. 218(3):472–479.
- 147 Cuevas P, et al. 1984. Pericyte endothelial gap junctions in human cerebral capillaries. *Anat Embryol (Berl)*. 170(2):155–159.
- 148 Tilton RG, Kilo C, Williamson JR. 1979. Pericyte-endothelial relationships in cardiac and skeletal muscle capillaries. *Microvasc Res*. 18(3):325–335.
- 149 Tigges U, Boroujerdi A, Welser-Alves JV, Milner R. 2013. TNF- $\alpha$  promotes cerebral pericyte remodeling in vitro, via a switch from  $\alpha$ 1 to  $\alpha$ 2 integrins. *J Neuroinflammation*. 10(1):33.